Ab initio investigation of the Peierls potential of screw dislocations in bcc Fe and W

Lisa Ventelon [a,*], F. Willaime [a], E. Clouet [a], D. Rodney [b]

[a] *CEA, DEN, Service de Recherches de Métallurgie Physique, F-91191 Gif-sur-Yvette, France*
[b] *Science et Ingénierie des Matériaux et Procédés, Institut Polytechnique de Grenoble, CNRS/UJF, 38402 Saint Martin d'Hères, France*

Abstract

The easy, hard and split core configurations of the $\langle 111 \rangle$ screw dislocation and the energy pathways between them are studied in body-centered cubic (bcc) Fe and W using different density functional theory (DFT) approaches. All approaches indicate that in Fe, the hard core has a low relative energy, close to or even below that of the saddle configuration for a straight path between two easy cores. This surprising result is not a direct consequence of magnetism in bcc Fe. Moreover, the path followed by the dislocation core in the (111) plane between easy cores, identified here using two different methods to locate the dislocation position, is almost straight, while the energy landscape between the hard core position and the saddle configuration for a straight path is found to be very flat. These results in Fe are in contrast with predictions from empirical potentials as well as DFT calculations in W, where the hard core has an energy about twice that of the maximum energy along the Peierls barrier, and where the dislocation trajectory between easy cores is curved. Also, the split core configuration is found to be unstable in DFT and of high energy in both Fe and W, in contrast with predictions from most empirical potentials.
© 2013 Acta Materialia Inc. Published by Elsevier Ltd. All rights reserved.

Keywords: DFT calculation; Screw dislocation; Peierls potential; Body-centered cubic metals

1. Introduction

It is well known experimentally in body-centered cubic (bcc) Fe [1–4], and more generally in all bcc transition metals [5–7], that non-screw dislocations have a much higher mobility than screw dislocations, and that the $\langle 111 \rangle \{110\}$ slip system dominates at low temperature. The unusual low-temperature plastic behavior of the $\langle 111 \rangle$ screw dislocations in bcc transition metals has long been attributed to their core structure, which offers a high lattice-friction stress. The lower mobility of screw dislocations and their $\{110\}$ glide plane have recently been corroborated by in situ transmission electron microscopy tensile experiments in ultra-high-purity α-Fe [8].

The $\langle 111 \rangle$ screw dislocations in bcc transition metals have been modeled using various atomistic schemes such as pair potentials [9,10], N-body potentials [11–18], bond-order potentials [19,20] and density functional theory (DFT) methods [21–30]. Two types of cores can be obtained by centering the dislocation in between three $\langle 111 \rangle$ atomic columns, depending on the sign of the Burgers vector, or equivalently on the orientation of the triangle formed by the three $\langle 111 \rangle$ columns: an easy core, where the chirality of the $\langle 111 \rangle$ columns is reversed compared to outside the core, and a hard core, where the $\langle 111 \rangle$ columns are at the same level. All the above-mentioned atomistic simulations exhibit the easy core configuration as the most stable. All DFT studies performed so far in pure metals have evidenced that the easy core structure is symmetric—or non-degenerate—i.e. close to elasticity theory [21–24,26,28,31], at variance with most empirical potentials. However, it should be noted that alloying W with Re was

---

* Corresponding author. Tel.: +33 1 69 08 11 77; fax: +33 1 69 08 68 67.
  E-mail address: lisa.ventelon@cea.fr (L. Ventelon).

recently predicted to induce a symmetry breaking of the core, yielding a degenerate core structure [27,29]. A third type of dislocation core morphology was proposed using interatomic row potentials, the so-called 'split' core [32,33]. It corresponds to a configuration where the 3-fold symmetry is broken and the relative displacements of the three atomic columns around a hard core triangle are $b/2$, $b/2$ and 0, where b is the Burgers vector. The dislocation center determined from the elastic strain field away from the core region is then situated in the immediate vicinity of an atomic column. Takeuchi et al. found, using parameterized interatomic row potentials, that the split configuration is systematically metastable when the easy core is non-degenerate, while it is unstable when the easy core is degenerate [33].

The elementary process associated with dislocation glide in a {110} plane corresponds to a translation between two easy core positions. DFT calculations of the corresponding Peierls barrier in Fe have evidenced a single hump barrier, at variance with the Takeuchi rule mentioned above [28,30,34] (indeed, the Peierls barrier adopts a 'camel-hump' shape with a local minimum between Peierls valleys when the split core is metastable, see below for details). Other DFT calculations of the Peierls barrier that exhibit a single hump shape were reported in bcc W and W alloys [35,36]. We note that the Takeuchi rule holds for pair and embedded-atom method (EAM) potentials in most cases [28,37,30,34], but is not a consequence of the lack of angular dependence of interatomic potentials since it has recently been found possible to parameterize EAM potentials for Fe and W, which reproduce the expected single-hump Peierls barrier with a non-degenerate core structure [35,18]. The single hump shape of the Peierls barrier has important consequences, in particular on the kink-pair formation mechanism [38].

The above studies focused on the one-dimensional path of the screw dislocation between stable configurations. The aim of the present paper is to gain insight into the two-dimensional Peierls potential, which governs plastic anisotropy [39], by characterizing from first-principles calculations the energetics of the easy, hard and split cores as well as the energy pathways between them. Due to the symmetry of the bcc lattice, the easy, hard and atomic row positions are expected to be energy extrema, assuming that the two-dimensional Peierls potential is continuous and differentiable. Easy cores are clearly minima, but the nature of the extremum at the hard core position and the topology of the Peierls potential near the split core are unclear. In the simple two-dimensional sinusoidal Peierls potential model of Edagawa et al. [40], if hard cores are maxima, then the saddle configuration between easy cores is necessarily close to a $\langle 111 \rangle$ column, i.e. close to a split configuration. However, the actual shape of the Peierls potential is obviously more complex. For instance, DFT calculations in Fe rule out the split configuration as a saddle point [30], and in Ta they suggest that the hard-core configuration might be a local minimum [41,21]. Moreover the metastable split configuration is degenerate with three

variants, thus invalidating a simple single-valued Peierls potential near the split-core configuration.

In order to explore the two-dimensional Peierls potential and notably the possible pathways for the dislocation to move from one minimum to the next, the energies of the easy, hard and split cores, along with the energy pathways between them, are investigated in Fe using DFT methods. Central to this study is an accurate determination of the dislocation position, allowing the Peierls stress to be estimated from the slope of the Peierls potential. Here we propose and compare two methods to locate the dislocation core. In addition, three empirical potentials for Fe are benchmarked against the DFT two-dimensional energy landscape, namely the Mendelev and Gordon EAM potentials [42,43], and a newly developed EAM potential denoted MCM2011 hereinafter [18]. The surprising results obtained in Fe are then compared to similar DFT calculations performed in bcc W.

2. Methodology

The present first-principles electronic structure calculations were performed within the DFT framework using mostly the PWSCF plane-wave code [44], with the projected augmented wave (PAW) method in Fe and the ultrasoft pseudopotential scheme in W. A wavefunction cut-off of 40 Ry (respectively 20 Ry) was used in Fe (respectively W). Additional calculations were performed using the DFT SIESTA code [45], as in a preliminary study in Fe [28]. This code was chosen for its efficiency stemming from the use of localized basis sets to investigate the robustness of the DFT results with respect to cell size and boundary conditions. We treated the $4s$, $4p$ and $3d$ (respectively $6s$, $6p$ and $5d$) states of Fe (respectively W) as valence states. The SIESTA pseudopotentials and basis sets for Fe and W have previously been validated by comparison with the generalized stacking fault energies and point defect calculations obtained with PWSCF [46,47]. The calculations in Fe are spin-polarized (ferromagnetic Fe) and the Perdew–Burke–Ernzerhof generalized gradient approximation (GGA)—which is known to perform better for the bulk properties in Fe—is compared to the local density approximation (LDA) with PWSCF and SIESTA. The Hermite–Gauss scheme to broaden the electronic density of states was used with a smearing of 0.3 eV. Residual forces after relaxation are smaller than 0.01 eV/Å.

Most of the dislocation calculations presented here were performed using a periodic array of dislocation dipoles [48], after comparison with a cluster geometry. Within the cluster model, a single dislocation is placed at the center of a finite cylinder and the surface atoms are fixed to the positions predicted by the anisotropic elasticity theory. The main drawback of this geometry lies in the difficulty within DFT to separate the energy due to surface contribution from the energy due to dislocation contribution. Thus the use of a cell, which guarantees that the surface contribution does not change along the path, or at least

between the initial and final states, was favored in the present work. Within the dipole approach, the use of tri-periodic boundary conditions is rather advantageous for electronic structure calculations and the elastic interactions between dislocations can be modeled by anisotropic elasticity [49,50]. The energetics is therefore well controlled within this geometry. Moreover, convergence is reached for a similar number of atoms per cell compared to the cluster approach. It is indeed at first sight doubled but more atoms are needed at the boundary in the cluster approach.

Two types of dipole geometries have been proposed for the $\langle 1\,1\,1 \rangle$ screw dislocation in bcc metals: the triangular [24] and quadrupolar [51,52,21] periodic arrays of dislocation dipoles. The former strictly preserves the 3-fold symmetry of the bcc lattice, while the latter leads to zero stress at any dislocation center thanks to the resulting square-like superposition of the elastic stress fields [48,31]. The quadrupolar arrangement actually appears to be the most appropriate to extract dislocation properties from supercell simulations with high accuracy [53,51,31]. In the present study, we used cells containing 135 and 273 atoms (Fig. 1). The cell vector length along the dislocation line is set to one Burgers vector $b = \frac{\sqrt{3}}{2} a_0$, where a_0 is the equilibrium lattice constant, i.e. $b \approx 2.47$ Å within the PWSCF GGA in Fe. Within this quadrupolar geometry, the dislocations constituting the dipole in the 135 (respectively 273) atom supercell in Fe are separated by approximately 17 Å (respectively 24 Å) in their glide plane.

The supercell vectors for the easy core configuration within a periodic quadrupolar arrangement (corresponding to $\vec{b} = \frac{1}{2}[1\,1\,1]$ in Fig. 1) are defined from the unit vectors $\vec{a}_1 = \frac{1}{3}[\bar{1}\,\bar{1}\,2]$, $\vec{a}_2 = \frac{1}{2}[1\,\bar{1}\,0]$ and $\vec{a}_3 = \frac{1}{2}[1\,1\,1]$ by the following expressions:

$$\vec{C}_1 = n\vec{a}_1 - \frac{1}{3m}\vec{a}_3,$$
$$\vec{C}_2 = \frac{n}{2}\vec{a}_1 + m\vec{a}_2 + \left(\frac{1}{2} - \frac{1}{6m}\right)\vec{a}_3, \qquad (1)$$
$$\vec{C}_3 = \vec{a}_3.$$

The $-\frac{1}{3m}$ and $-\frac{1}{6m}$ components along $\vec{a}_3$ come from the $\frac{\sqrt{2}}{6}a_0$ shift along $[1\,\bar{1}\,0]$ of the centers of gravity of the upward- and downward-pointing triangles. The 135 (respectively 273) atom supercell corresponds to integers $(n, m) = (15, 9)$ (respectively $(n, m) = (21, 13)$), as explained in Ref. [28]. The hard-core configuration can be obtained from the easy core one, either by changing the sign of the Burgers vector ($\vec{b} = \frac{1}{2}[\bar{1}\,\bar{1}\,\bar{1}]$ in Fig. 1), or by keeping the same sign of the Burgers vector and displacing the two dislocations to the adjacent triangles in the same $[\bar{1}\,\bar{1}\,2]$ direction. In the former case the components of $\vec{C}_1$ and $\vec{C}_2$ along $\vec{a}_3$ are reversed, while in the latter case one must account for the small homogeneous strain induced by the displacements perpendicular to $[\bar{1}\,\bar{1}\,2]$, of opposite signs and magnitude $\frac{\sqrt{2}}{6}a_0$ that both dislocations undergo when changing triangles. In this case the cell vectors are:

$$\vec{C}_1 = n\vec{a}_1 + \frac{1}{3m}\vec{a}_3,$$
$$\vec{C}_2 = \frac{n}{2}\vec{a}_1 + m\vec{a}_2 + \left(\frac{1}{2} + \frac{1}{6m}\right)\vec{a}_3, \qquad (2)$$
$$\vec{C}_3 = \vec{a}_3.$$

Convergence of the Peierls barrier with respect to the k-point grid was investigated with SIESTA and a 135-atom supercell, using $1 \times 2 \times 16, 2 \times 2 \times 16$ and $3 \times 3 \times 16$ shifted k-point grids. The $1 \times 2 \times 16$ grid yields Peierls barrier energies converged within 1 meV/b, and it was therefore used for this study.

In agreement with previous DFT calculations in Mo, Ta, Fe and W bcc metals [27,26,24,41,23,28,30], the stable core structure of the $\langle 1\,1\,1 \rangle$ screw dislocation in Fe and W is the non-degenerate easy core structure, for both exchange–correlation functionals, GGA and LDA. The core is completely unpolarized and no metastable polarized core is evidenced [46].

Given the complexity of the energy landscape, the possible impact of methodological choices on the calculation of the Peierls barrier was evaluated, in particular the localized basis set used for the DFT calculations in Ref. [28] is
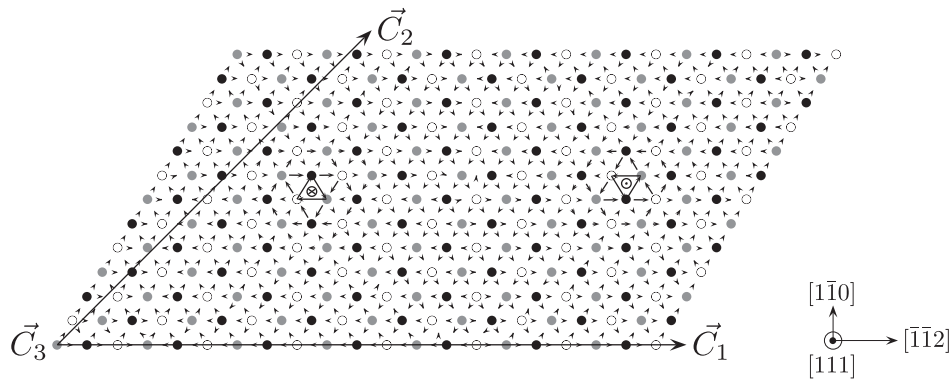

Fig. 1. Schematic representation of the unit cell and periodicity vectors within the quadrupolar arrangement (273 atoms). Atomic positions are represented by three different colors to emphasize the fact that they belong to three different $\langle 1\,1\,1 \rangle$ planes before introduction of the dislocations. The dislocation dipole is visualized by its differential displacement map. The upward-pointing triangle corresponds to $-\vec{b}$ dislocation core and the downward-pointing triangle, to $\vec{b}$ dislocation core. $\vec{b} = \frac{1}{2}[1\,1\,1]$ for the easy core configuration and $\vec{b} = \frac{1}{2}[\bar{1}\,\bar{1}\,\bar{1}]$ for the hard core configuration.
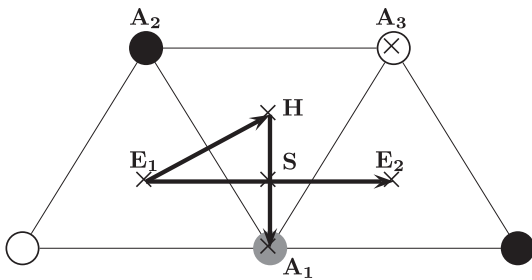
Fig. 2. Schematic representation of the three directions of the Peierls potential that were sampled: the energy barrier joining two neighboring easy-core positions (denoted E_1 and E_2); the energy barrier going from an easy- to a hard-core position (denoted H); and the energy barrier going from a hard-core position to a split-core position. The S point denotes the position halfway through the vector joining the two easy-core positions. The points A_1, A_2 and A_3 are centered on $\langle 111 \rangle$ atomic columns.
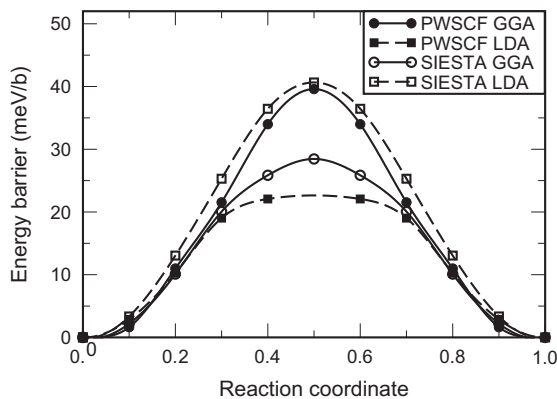

Fig. 3. Peierls barrier obtained in Fe within DFT using SIESTA and PWSCF, and two exchange–correlation functionals, GGA and LDA, in a 135 atom dipolar cell. The reaction coordinate method is used for finding saddle points.

compared with plane-wave basis sets. The energy barrier calculations joining two adjacent easy core configurations (denoted E_1 and E_2 in Fig. 2) were performed by displacing simultaneously the two dislocations such that their separation distance remains constant. The minimum energy path was then obtained using the reaction coordinate method [54], whereby the path was discretized in nine replicas initially linearly interpolated between the initial and final configurations, and the energy of each image was minimized in the hyperplane perpendicular to the initial path.

As shown in Fig. 3, all DFT approaches lead to single-hump Peierls barriers, thus confirming previous DFT results [28]. Note, however, that the amplitudes of Peierls barriers obtained with the different DFT approaches differ from one another. The effect of the exchange–correlation functional is unusually large near the saddle configuration: with PWSCF the Peierls energy is reduced by approximately 40% from GGA to LDA. The origin of this surprisingly strong effect, which is likely to be coupled to magnetism, as described in Section 4, requires further investigation. Within SIESTA, the effect of the exchange–correlation functional is reversed. A similar discrepancy

between the PWSCF and SIESTA results on the effect of the exchange–correlation functional was also observed when calculating the generalized stacking faults [46]. Also, it is seen that the SIESTA results, previously published in Ref. [28], underestimate the Peierls barrier, probably because the use of reduced localized basis sets and the pseudopotential approximation lead to a less accurate description of magnetism. The best estimate of Peierls energy is 40 ± 5 meV/b (PWSCF GGA).

As shown in Ref. Appendix A, we checked the validity of the simple reaction coordinate method used here [54], which is sometimes questioned [43], by comparing the resulting minimum energy path with the more computationally demanding nudged elastic band (NEB) method [55]. In the case of the present paths, which are rather simple and straight in configuration space in comparison, for example, to kink formation processes [56], the reaction coordinate method determines correctly the energy path. A difference remains between the reaction coordinate and NEB paths, but the latter is within the uncertainty range of the present calculations (about 5 meV/b). The reaction coordinate method, which is easier to implement than the NEB method, makes the calculations up to one order of magnitude faster because: (i) only half of the Peierls barrier needs to be computed; (ii) the relaxation over every image is more efficient thanks to the use of conjugate gradient type methods; and (iii) it allows a sequential minimization of the images along the path rather than a global minimization. As a result, we will mostly use this method in the following.

The effect of cell geometry and size was also investigated using the SIESTA GGA. The Peierls barrier was calculated within the cluster approach, centering the cluster supercell on the S point, as defined in Fig. 2, so as to ensure that the surface contribution to the energy is the same for the initial and final states assuming that its variation can be neglected in between. The SIESTA result using a 261-atom cluster is compared to the Peierls barrier obtained in the dipole approach using 135 and 273 atoms (Fig. 4). Neither the
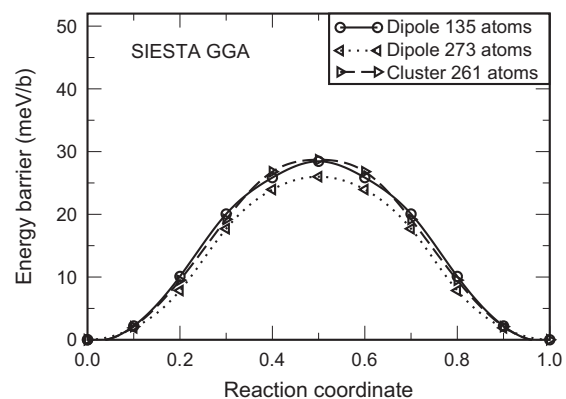

Fig. 4. Effect of the cell geometry (cluster vs. dipole) and of the cell size on the Peierls barrier obtained in Fe with SIESTA GGA using the reaction coordinate method.

single-hump shape nor the barrier amplitude change significantly with the size and geometry of the simulation cell, the energy differences remaining within the uncertainty range of the calculations.

3. Two-dimensional Peierls potential in Fe

3.1. Peierls barrier

The DFT calculations of the one-dimensional Peierls barrier in Fe evidenced a single-hump Peierls barrier with no intermediate metastable core configuration. Three representative empirical potentials for Fe were benchmarked against the present DFT results, namely the widely used EAM potential obtained by Mendelev et al. [42], which includes DFT point defect properties in its fit, the more recent EAM potential developed by Gordon et al. [43], who supplemented the fitting properties with a DFT Peierls barrier, and the newly developed MCM2011 EAM potential, which correctly reproduces the expected single-hump Peierls barrier, as described in the supplementary materials of Ref. [18]. As shown in Fig. 5, the Mendelev potential yields a Peierls barrier, a factor of 4 smaller than the PWSCF GGA, and with a double-hump shape and a halfway metastable core configuration, which corresponds to the split-core configuration, as reported in the literature [57,37,58,38,43], and in agreement with the Takeuchi rule mentioned in the Introduction. Gordon potential does not improve significantly the Peierls barrier: the intermediate metastable state is less pronounced but the height of the Peierls barrier is in similar disagreement with the DFT calculations. The split configuration has an energy about 6 meV/b (respectively 11 meV/b) higher than the easy core with Mendelev (respectively Gordon) potential. In order to investigate whether a similar local minimum exists on the DFT Peierls potential, a relaxation was performed using SIESTA, starting from the atomic positions of the split core obtained with Mendelev potential. During the relaxation, the dislocation spontaneously transformed into an
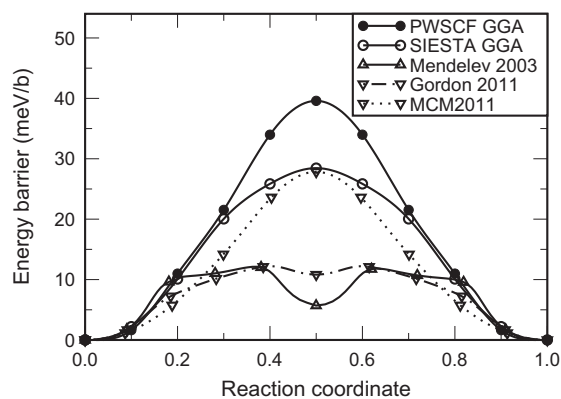

Fig. 5. Peierls barrier calculated in Fe with PWSCF GGA using the reaction coordinate method, compared to EAM potential calculations using Mendelev [42], Gordon [43] and MCM2011 potentials [18], with the NEB method.

Table 1
Energy (in meV/b) of the hard-core, saddle and split-core configurations with respect to the easy-core configuration, in Fe using the different energetic models. The DFT energies are given ±5 meV/b.

	Hard	Saddle	Split
PWSCF GGA	39	40	
PWSCF LDA	23	22	
SIESTA GGA	23	29	79
SIESTA LDA	45	40	
Mendelev 2003	176	12	6
Gordon 2011	115	12	11
MCM2011	63	28	33

easy core, thus confirming that the local minimum at the metastable split core configuration is an artifact of these potentials. On the other hand, the MCM2011 potential does not exhibit such an intermediate metastable configuration, showing that a metastable split configuration is not a necessarily corollary of a non-degenerate core modeled with an EAM potential. The Peierls barrier with this potential, which was fitted using the SIESTA GGA results, is about 28 meV/b (see Fig. 3).

3.2. Hard-core configuration

The nature of the extrema at the hard-core position (denoted H in Fig. 2) was investigated within DFT. The hard core, even if unstable, can be stabilized numerically. A constrained minimization was performed such that the positions along $\vec{b}$ of the three central atomic columns constituting the hard-core structure were kept fixed, while all other degrees of freedom were relaxed [30]. If, following this pre-relaxation, the constraint is released in order to fully relax the hard-core configuration, depending on the energetic model, the hard-core may relax to an easy-core configuration, but it may also remain in a hard-core position with an energy decrease of less than 1 meV/b. The pre-relaxed configuration can therefore be considered as a good approximation of the relaxed hard-core configuration.

The energy differences between the hard- and easy-core structures obtained in Fe within DFT are given in Table 1. They are compared to the saddle-point energy obtained from the Peierls barrier calculation; as shown in Section 3.4, this saddle configuration is positioned close to the S point in Fig. 2. Within DFT, a significant scatter is observed as a function of the calculation scheme, but it is striking to see that, for a given calculation scheme, the energies of both the hard-core position and saddle configuration for the straight path are very close and within the numerical uncertainty estimated at ±5 meV/b, as reported in Ref. [30].

The hard-core structure is often regarded as irrelevant for dislocation motion because its energy is expected to be much higher than the Peierls energy, an assumption based on steric considerations corroborated by empirical potential calculations. The present investigation shows, on the contrary, that the hard-core and saddle configuration energies are similar in Fe according to DFT.

With the Mendelev and Gordon potentials, on the other hand, the hard-core configuration is highly unfavorable, while it is less unfavorable with the MCM2011 potential, as shown in Table 1. The energy difference between easy- and hard-core structures is indeed overestimated by a factor of more than 4 with the Mendelev potential, and by almost 3 with the Gordon potential, compared to the PWSCF GGA result. The MCM2011 potential yields a more satisfactory agreement with DFT estimate, with an overestimation of approximately 50%.

More insight into the energy variation around the hard-core position was gained by investigating the pathway going from an easy-core configuration to a neighboring hard-core configuration. In this calculation, the cell shape was kept fixed between the initial state, the easy-core configuration centered on the E_1 point, and the final state, the hard-core configuration centered on the H point (Fig. 2). Thus the elastic strain between the initial and final states is different. The resulting elastic contribution to the energy estimated using anisotropic elasticity theory is, however, less than 5 meV/b for the 135-atom cell, and therefore within numerical uncertainty. The energy barriers obtained with DFT, as well as with empirical potentials, are represented in Fig. 6a. In the DFT case, the energy variation is similar to that along the Peierls barrier. In particular, no local minimum is found around the hard core, unlike what was reported for Ta in Ref. [41]. In the case of the Mendelev and Gordon potentials, the hard core corresponds to an energy maximum so high that within the dipole approach, the relaxed path deviates from the high symmetry line joining the easy and hard cores (both with the reaction coordinate and NEB methods). For this reason, in Fig. 6a the Mendelev and Gordon potential results are plotted using the cluster approach, where this difficulty does not arise for symmetry reasons. This problem did not appear with MCM2011, the hard core corresponding to a lower energy maximum. Fig. 6a evidences a better agreement with DFT of the MCM2011 potential results than the Mendelev and Gordon potential results.

3.3. Split-core configuration

When taking the atomic arrangement into account, the topology of the Peierls potential around atomic row positions, noted A_i ($i = 1, 2, 3$) in Fig. 2, appears to be quite complex, and a detailed description is beyond the scope of the present paper. With the Mendelev and Gordon potentials, three different variants of the 2-fold symmetry metastable split core are centered very close to a given atomic row. The Peierls potential can therefore be viewed as multivalued near the A_i point, depending on the variant considered.

An estimate of the energy close to the atomic rows was obtained from the split-core configuration [30]. The split core was generated from the hard core by adding a relative displacement along $\vec{b}$ of $b/6$ to A_2 and $-b/6$ to A_3 (Fig. 2), in order to have no relative displacement between these two
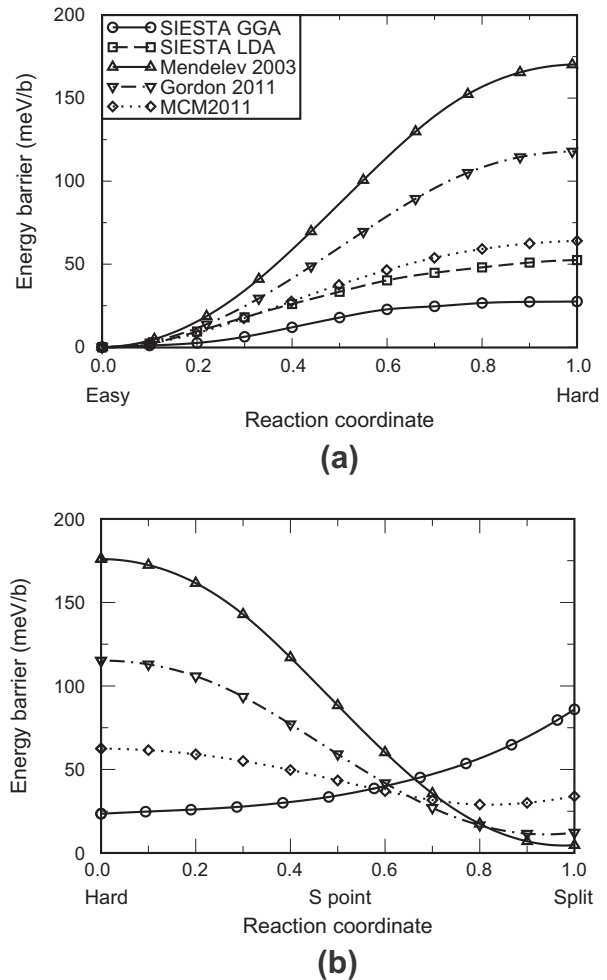

(a)

(b)

Fig. 6. Energy variation in Fe between (a) the easy- and hard-core structures and (b) the hard- and split-core structures calculated within DFT using SIESTA and compared to empirical potential calculations using the Mendelev, Gordon and MCM2011 potentials, within the quadrupolar arrangement. The reaction coordinate in (b) is defined as: $1 - \frac{\delta z}{b/3}$, where δz is the relative displacement along $\vec{b}$ between columns A_2 and A_3 (Fig. 2), so that $\delta z = 0$ for the split core and $\delta z = b/3$ for the hard core. The elastic correction was neglected.

columns, which is a characteristic of the fully split core. The same constrained minimization as the one used to stabilize the hard core was then used to relax the split-core structure, i.e. by freezing the displacements along $\vec{b}$ of A_1, A_2 and A_3. As shown in Table 1, SIESTA GGA calculations evidence a high split-core energy, with an excess energy with respect to the easy-core structure of 79 ± 5 meV/b in a 273-atom cell, in agreement with other DFT calculations [30]. The split-core configuration therefore has a much higher energy than the easy-core structure within DFT. On the other hand, the same calculations performed with the Mendelev and Gordon potentials yield excess energies very close to that of the metastable split core, i.e. about 6 and 11 meV/b respectively. The MCM2011 potential is again closer to DFT, with an excess energy of about 33 meV/b, i.e. close to the Peierls energy.

The energy variation along the ridge separating the energy basins centered on E_1 and E_2 was investigated from

the pathway going from the hard-core to the split-core configurations. The energy along the path was obtained by a minimization using the same constraint as for the hard and split cores, i.e. by fixing the components along $\vec{b}$ of A_1, A_2 and A_3. The DFT energy landscape is shown to be rather flat between the hard-core and saddle configurations, at variance with the EAM potentials (Fig. 6b). Again the MCM2011 potential is in better agreement with DFT, although like the other EAM potentials, it predicts a higher energy for the hard-core configuration than for the split-core configuration. The DFT energy landscape therefore suggests that the dislocation may have similar probabilities of passing anywhere between the hard core and the straight path between easy cores. The hard core may even be the lowest in energy, and it cannot be ruled out that it is the true saddle point. This would then correspond to a so-called monkey-type saddle [59].

The DFT results suggest that there should be maxima of the Peierls potential at the atomic row positions, A_i. It is striking that the same conclusion was proposed by Edagawa et al. [39] in order to account for the absence of asymmetry in the crystal orientation dependence of the critical flow stress observed experimentally in Fe at low temperature [60]. Second-order harmonic terms were included in the Fourier expansion describing the two-dimensional Peierls potential in order to obtain this feature.

3.4. Dislocation core position

The Peierls stress is related to the maximum derivative of the Peierls barrier with respect to the dislocation core position. This implies that the Peierls barrier has to be sought as a function of the dislocation core position, which a priori does not correspond exactly to the reaction coordinate used in the constrained relaxation. Methods to identify the dislocation core position have been proposed [57,61,62]. Here the position of the dislocation center

was determined using two different methods described in Ref. Appendix B. The first method consists in comparing the relative displacements of the five most displaced $\langle 111 \rangle$ atomic columns [61] with that of the anisotropic elastic displacement field Section B.1. The resulting cost function defined in Eq. (B.1) is minimized with respect to the dislocation core position in the $(1\,1\,1)$ plane. We considered another method, which consists in comparing the disregistry that corresponds to the difference of displacement between the two {1 1 0} atomic planes situated directly above and below the glide plane with solutions of an elastic model similar to the Peierls–Nabarro model Section B.2. The disregistry in the direction of the Burgers vector computed with DFT was adjusted to Eq. (B.6) through the fitting parameters x_1 and y_1, i.e. the dislocation core position in the $(1\,1\,1)$ plane.

These two methods were first tested on the linear interpolation of Cartesian atomic coordinates between initial and final positions, two neighboring easy-core positions, obtained within anisotropic elasticity prior to relaxation. The resulting dislocation core positions in the glide plane (projection on the $(1\,\bar{1}\,0)$ plane) are represented in Fig. 7a as a function of the reaction coordinate. It should be noted that the two fitting procedures naturally find exactly the easy-core position in the initial and final states. On the other hand, the dislocation-core position obtained with both methods deviates from the dislocation-core position proportional to the reaction coordinate.

The cost and disregistry function methods were then used to determine the dislocation-core position in the glide plane after relaxation from the DFT atomic positions along the Peierls barrier shown in Fig. 3. Both methods predict the same dislocation path, with non-negligible deviations from the dislocation core position proportional to the reaction coordinate (Fig. 7b). The DFT relaxation reverses the deviation in such a way that the dislocation core prefers to remain within the energy minima in the energy landscape [61].
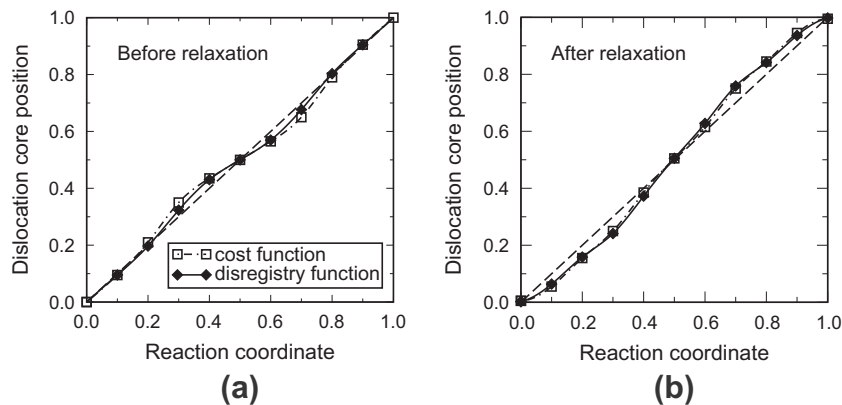

Fig. 7. Dislocation-core position as a function of the reaction coordinate in Fe extracted from (a) linear interpolation of atomic coordinates between initial and final positions obtained within anisotropic elasticity prior to relaxation, and (b) the PWSCF GGA results after relaxation using the reaction coordinate method with the 135-atom cell. The method to determine the dislocation-core position using the cost function method (squares) is compared to the disregistry function method (diamonds). The dashed line shows the dislocation-core position along the glide plane proportional to the reaction coordinate. The dislocation-core position is normalized by $\sqrt{\frac{2}{3}}a_0$.

The trajectory obtained for the dislocation center in the (1 1 1) plane as the dislocation translates from one easy-core position to another easy-core position is almost a straight line in Fe within DFT, as shown in Fig. 8a and c for both methods for finding the dislocation-core position and for all DFT schemes. In particular halfway along the path, the dislocation is centered close to the middle of E_1 and E_2, denoted S in Fig. 2.

The same approaches applied to the Mendelev potential yield a trajectory that is not straight, but curved with a cusp halfway along the path (Fig. 8b and d). This is because the path passes through the split configuration as mentioned above, which is centered close to the A_1 point. However, it should be noted that with the cost function method, the associated value of the cost function is higher by about 2 orders of magnitude compared to its value in the initial and final states, indicating a significant deviation from elasticity. For comparison, the midway cost function value within DFT is of the same order of magnitude as at the initial and final states. The estimation of the dislocation core position is therefore less reliable in the case of the Mendelev potential. Nonetheless the two methods for finding dislocation core positions evidence a deviation of the dislocation core trajectory from the DFT straight line, related to the double-hump Peierls barrier and the metastable split-core configuration.

From these fitting procedures, the Peierls barrier can be represented as a function of the dislocation-core position. The two fitting methods result in comparable Peierls barriers as a function of the dislocation-core position, shown in Fig. 9. On the other hand, the shape of the Peierls barrier is significantly different when the energy is plotted as a function of the reaction coordinate.
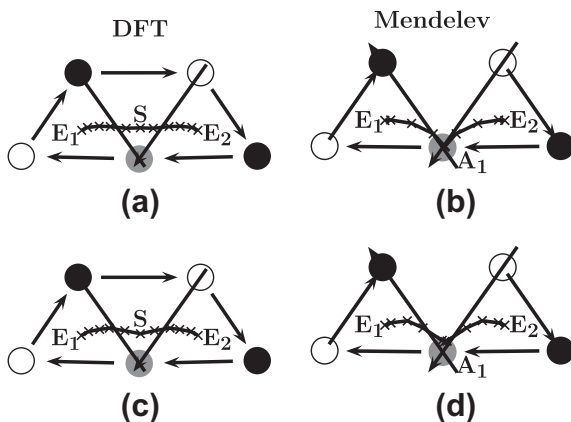

Fig. 9. Peierls barrier calculated in Fe with the PWSCF GGA using the reaction coordinate method and 135 atoms, vs. the reaction coordinate, ξ (circles) and vs. the dislocation core position, x, calculated either with the cost-function method (squares) or the disregistry method (diamonds). The dislocation core position, x, is normalized by $\sqrt{\frac{2}{3}}a_0$.

The Peierls stress can be estimated from the maximum slope of the Peierls barrier, based on the hypothesis that the stress dependence of the Peierls barrier can be neglected [57]. This straightforward method was applied to the Peierls barriers represented in Fig. 9. The estimated Peierls stress extracted from the PWSCF GGA results amounts to 1.4 ± 0.1 GPa with both disregistry and cost-function methods. These results are all consistent with one another and evidence the usual discrepancy between atomistic and experimental estimates of the Peierls stress, i.e. about 400 MPa at 5 K [63]. Ref. [18] suggests that this discrepancy is due to quantum effects. It should be noted that by fitting the Peierls barrier with a sinusoidal function, the Peierls stress also amounts to about 1.4 GPa. This simple approximation is thus relevant in this high-symmetry case, for which we do not expect any asymmetric shape or subsidiary minimum in the Peierls barrier. Comparable Peierls stresses of 1.1 ± 0.1 GPa were obtained with the SIESTA GGA either within the sinusoidal approximation or using the maximum slope of the Peierls barrier. Since hard-core and saddle-point configurations have similar energies, as seen previously, the Peierls stress was also estimated from the maximum slope of the energy barrier between the hard- and easy-core configurations, calculated as a function of dislocation-core position, and amounts to about 1.1 GPa with the SIESTA GGA, i.e. in the same range as the value extracted from the energy barrier between two easy-core configurations. This result again does not rule out the hard-core configuration as a potential saddle point for dislocation motion in Fe.

4. Specific behavior in Fe

4.1. Comparison between bcc Fe and W

In view of the unexpected results obtained within DFT for Fe, in particular the low relative energy of the hard

Fig. 8. Trajectory followed by the dislocation center in the (1 1 1) plane in Fe when passes over the Peierls barrier calculated using the cost function minimization from (a) the PWSCF GGA and (b) the Mendelev potential results, and using the disregistry function method from (c) the PWSCF GGA and (d) the Mendelev potential results. The atomic positions and the differential displacement maps correspond to the dislocation core structure halfway along the path. The difference obtained on these maps between DFT and the Mendelev potential is related to a dislocation core centered either on the S or the A_1 point.
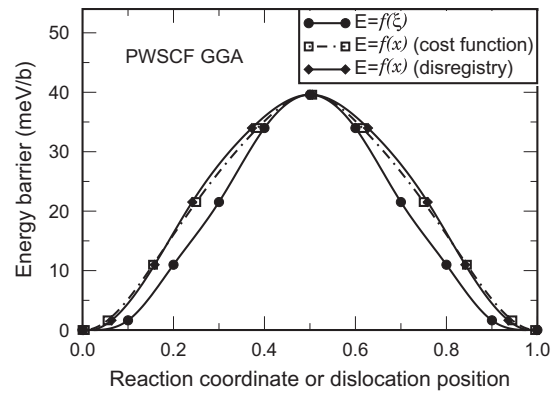
core, and because of the large discrepancies observed between DFT and empirical potentials, the main calculations were repeated in W, in order to discriminate between what is likely to be either specific to Fe or common to all bcc transition metals.

First, the energy barrier joining two adjacent easy-core configurations in W has, as in Fe, a single hump shape according to DFT (Fig. 10). The Peierls barrier amplitude amounts to about 90 meV/b (respectively 70 meV/b) using the PWSCF GGA (respectively SIESTA GGA), in good agreement with another estimate of the Peierls barrier from DFT calculations [36]. The effect of the exchange–correlation functional is less pronounced than in Fe: with SIESTA, the Peierls energy is about 10% larger with LDA than with GGA (Fig. 10). The trajectory followed in W by the dislocation center in the (1 1 1) plane is less straight than in Fe, probably to avoid the hard-core position, which has a higher relative energy, as seen in Table 2 (inset of Fig. 10). The Peierls stress was estimated in the same way as in Fe, i.e. from the maximum slope of the Peierls barrier as a function of the dislocation-core position, and using both methods for finding the dislocation-core position. DFT Peierls barriers yield comparable Peierls stresses ranging from 1.9 to 2.2 GPa. As already pointed out in Fe, the atomistic estimates of the Peierls stress in W evidence the usual discrepancy with the experimental value, i.e. about 800 MPa at 26 K [64].

The hard-core energy was calculated with DFT and the results are summarized in Table 2. They show that the

excess energy of the hard core amounts to about twice the saddle point with both exchange–correlation functionals. This result is different from the case of Fe, where these two energies are similar. Finally, the energy of the split core was estimated with SIESTA GGA and amounts to 176 ± 5 meV/b with respect to the easy-core configuration, i.e. three times the Peierls barrier value. As seen previously for Fe, the split core in W has therefore a much higher energy than the easy core.

4.2. Magnetism in Fe

Magnetism is often regarded as the driving force for explaining the specificity of the properties of Fe with respect to non-magnetic bcc transition metals [65]. We therefore investigated the local magnetic moments for various core configurations in Fe within DFT.

The local atomic magnetic moments are expected to be weakly perturbed by the presence of the screw dislocation since the coordination numbers and bond lengths are less affected than for other defects such as vacancies, interstitials or surfaces. This was corroborated by the analysis of the change in the local magnetic moment concentrating on the ⟨1 1 1⟩ atomic columns around the dislocation core in Fe, calculated using the Mulliken and Löwdin population analysis, within SIESTA and PWSCF, respectively, performed on 135-atom cells. We found that using PWSCF GGA the local magnetic moment close to the dislocation core is increased with respect to the bulk value (2.18 μ_B/atom) by 0.18 μ_B/atom in the easy-core configuration, as represented in Fig. 11a. A similar increase of the local
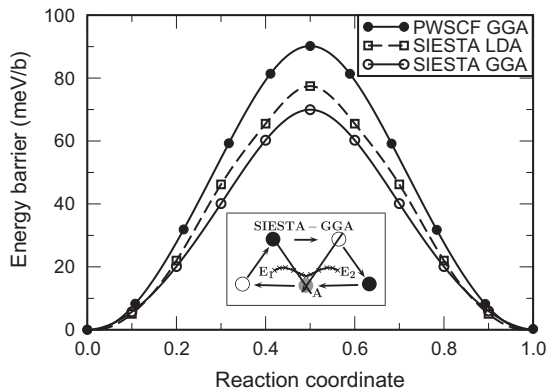

Fig. 10. Peierls barrier calculated in W with the SIESTA and PWSCF GGA (and also LDA for SIESTA). The calculations were performed using 135 (respectively 273) atoms and the NEB method (respectively the reaction coordinate method) for PWSCF (respectively SIESTA) calculations. The inset corresponds to the position of the dislocation when passing over the Peierls barrier calculated using the disregistry function method from the SIESTA GGA.

Table 2
Energy (in meV/b) of the hard-core, saddle and split-core configurations with respect to the easy-core configuration in W using the SIESTA GGA and LDA. The DFT energies are given ±5 meV/b.

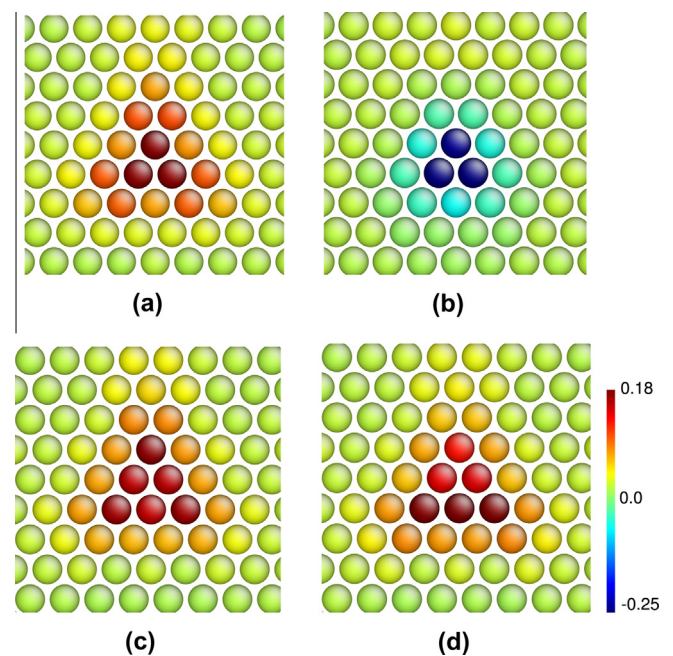|	Hard	Saddle	Split
SIESTA GGA	157	70	176
SIESTA LDA	153	77	

Fig. 11. Variation of the magnetic moment per atom, in Bohr magneton units, calculated in Fe within PWSCF in a 135-atom quadrupolar cell due to the presence of the dislocation in the easy-core configuration using (a) GGA and (b) LDA, (c) in the hard-core configuration with GGA and (d) in the halfway position with GGA.

magnetic moment was obtained with the SIESTA GGA, i.e. 0.20 μ_B/atom with respect to the bulk magnetic moment (2.32 μ_B/atom). This weak increase of about 0.2 μ_B/atom obtained both with the PWSCF GGA and the SIESTA GGA is in relatively good agreement with locally self-consistent multiple scattering calculations performed recently in bcc Fe [66]. The same analysis in the hard-core and saddle configurations evidences a similar weak increase of respectively 0.17 μ_B/atom and 0.18 μ_B/atom with the PWSCF GGA (Fig. 11c and d), and 0.22 μ_B/atom and 0.23 μ_B/atom with the SIESTA GGA. The total magnetic moment for these three configurations also evidence a weak increase from the bulk total magnetic moment of about 3 μ_B with the PWSCF GGA and 5 μ_B with the SIESTA GGA in the 135-atom supercell containing the dislocation dipole.

The effect of the exchange–correlation functional is significant. The PWSCF LDA and SIESTA LDA results reveal also a weak perturbation of the local atomic moments around the dislocation core, but with reversed sign: the magnetic moments around the easy-core structure are reduced with respect to the bulk value by about 0.2 μ_B/atom with the PWSCF LDA (Fig. 11b) and 0.1 μ_B/atom with the SIESTA LDA. A similar weak decrease of the magnetic moments was obtained around the hard-core and saddle configurations with both the PWSCF LDA and the SIESTA LDA. Other DFT calculations in Fe have also shown a reduction of the magnetic moment using the LDA approximation [24]. These reversed trends between the GGA and LDA approximations are compatible with the effect of the exchange–correlation functional on the change in total magnetic moment due to stacking faults [46]. Indeed, it was shown using both PWSCF and SIESTA that the average magnetic moment due to stacking faults in the {110} plane is enhanced with respect to the bulk in the GGA approximation, while it is reduced in the LDA approximation.

The easy-core, hard-core and saddle-point configurations were found to exhibit similar behaviors, suggesting that magnetism is not at the origin of the low energy of the hard-core configuration. On the other hand, the two exchange–correlation functionals predict opposite changes, with respectively a small increase and a small decrease of the magnetic moment with respect to the bulk. The coupling with magnetism may therefore explain part of the scatter observed in Fe between the LDA and GGA results in Table 1.

5. Conclusion

The work presented in this paper providesa quantitative description of the most relevant cross-sections in the two-dimensional Peierls potential of the ⟨111⟩ screw dislocation in bcc Fe and W from first-principles calculations. All DFT approaches yield a single-hump Peierls barrier with no intermediate metastable core configuration in Fe. In Fe, the Peierls barrier amounts to 40 ± 5 meV/b with

a plane-wave approach, higher than previous estimate based on a localized basis approximation. As the dislocation passes over the energy barrier between two adjacent easy-core configurations, its position in the (111) plane exhibits a nearly straight trajectory. The energy landscape between the hard-core and saddle positions is very flat. The DFT results do not preclude the hard-core as a potential saddle point in Fe and the dislocation may have comparable probabilities to pass anywhere in between the hard core and the straight path between easy cores. The unexpected low energy of the hard core suggests that this configuration has to be regarded as essential for dislocation motion in Fe. On the other hand, the split core exhibits a high energy in DFT calculations (about 79 meV/b).

The Mendelev and Gordon EAM potentials for Fe give the correct non-degenerate core structure but suffer from three main inadequacies: the Peierls barrier is low (about 12 meV/b); the hard-core structure is a high-energy maximum of the Peierls potential (110–180 meV/b); and the dislocation trajectory is not straight but passes through the split-core configuration, resulting in a double-humped Peierls barrier. The trajectory of the dislocation center when passing over the Peierls barrier deviates significantly from the DFT straight line, with a midway intermediate position that corresponds to the split-core configuration. Admittedly the dip of the camel hump obtained with the Gordon potential is less pronounced than with the Mendelev potential, but regarding the height of the Peierls barrier and the energy of the hard-core structure, these two empirical potentials show similar behaviors. In comparison, the MCM2011 potential for Fe is clearly in more satisfactory agreement with the DFT results, with a single-hump Peierls barrier of about 28 meV/b and an energy of the hard-core configuration of about 63 meV/b, although it is a maximum of the Peierls potential, at variance with DFT.

Comparison with the DFT Peierls potential of another bcc metal, W, shows two common features: the single-hump shape of the Peierls barrier, which amounts to 90 ± 5 meV/b, and the large energy of the split core. On the other hand, in W the energy of the hard-core configuration is about twice the Peierls energy. The low energy of the hard core is thus likely to be specific to Fe.

Comparable changes of the local magnetic moment were found around the easy-core, hard-core and saddle-point configurations in Fe. Therefore, magnetism alone does not explain directly the low energy of the hard-core configuration in Fe. Some discrepancies were evidenced between LDA and GGA on the local magnetic moment around the dislocation core, with respectively a small increase and a small decrease relative to the bulk.

The present DFT work shows that care must be taken when modeling the two-dimensional Peierls potential with a parameterized sinusoidal model, as proposed by Edagawa et al. [40] and recently employed by Gröger et al. to analyze BOP calculations [67]. Indeed, with this representation, if the hard core is a maximum of the Peierls potential, the dislocation path between easy cores passes necessarily

near atomic row positions. These constraints are not compatible with the present results in Fe, where the hard core has a low relative energy and the dislocation path runs approximately straight between easy cores. Qualitatively in Fe, the topology of the DFT Peierls potential is reversed compared to the simple two-dimensional sinusoidal model: the location of saddle point and maximum are indeed inverted or nearly inverted with unexpected flat regions. Higher-order harmonics should therefore be included in the two-dimensional Peierls potential representation to reflect the DFT results, including in W where the split core has also a high energy [39].

Acknowledgments

Appendix A. Saddle-point finding methods

Two methods for finding transition pathways and saddle points are compared using the PWSCF code: the reaction coordinate method (or drag method) [54] and the NEB method [55]. Within the reaction coordinate method, the Cartesian coordinates of all atoms in the system are used to define a reaction coordinate constraining the system to relax in the hyperplane perpendicular to the vector joining the initial and final states. The transition pathway is constructed starting from a discrete set of configurations interpolating between initial and final configurations, and carrying out a constrained minimization over the remaining degrees of freedom of the system. Within the NEB method, a chain of images is generated between initial and final states, with intermediate images connected between first neighbors with springs, and a global relaxation is performed. Relaxation was stopped when the forces perpendicular to the path are smaller than 0.02 eV/Å. The NEB method has already been used to calculate Peierls barriers using first-principles methods, e.g. in silicon [62]. In both methods the results were plotted as function of the reaction coordinate of the drag method, denoted ξ hereinafter. It is defined as the projection of the vector joining the current state to the initial state on the vector joining the final state to the initial state, normalized so as to vary between 0 and 1 along the reaction pathway. The Peierls barriers obtained with the reaction coordinate and the NEB methods are identical to within an uncertainty of about 5 meV/b, as shown in Fig. A.12.
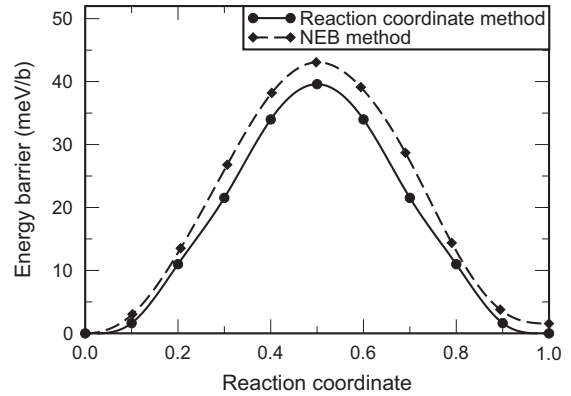

Fig. A.12. Comparison of the two methods for finding saddle points set up in the calculation of the Peierls barrier in Fe with PWSCF GGA using 135 atoms.

Appendix B. Determination of the dislocation-core position

B.1. Cost-function method

We define a cost function within the periodic distribution of dislocation dipoles based on the Volterra field to determine the centers (x_1, y_1) and (x_2, y_2) of the two dislocations constituting the dipole:

$$C(x_1, y_1, x_2, y_2) = \sqrt{\sum_{i=1}^{n} \left(\delta_{z_i} - \delta_{z_i}^{el}(x_1, y_1, x_2, y_2)\right)^2}. \quad (B.1)$$

In this expression, $\delta_{z_i}^{el}(x_1, y_1, x_2, y_2)$ is the anisotropic elastic displacement field of atom i induced by the dislocation dipole positioned at (x_1, y_1) and (x_2, y_2) and by its periodic images along the x and y directions, and δ_{z_i} is the displacement field as obtained in the atomistic simulations. The two dislocation cores are assumed to have simultaneous and equivalent displacements, i.e. (x_2, y_2) is set to $\left(x_1 + \frac{L}{2}, -y_1\right)$, where L is the length of the simulation cell along the glide plane $\left(L = n\sqrt{\frac{2}{3}}a_0\right)$. In the calculation of the energy barrier when going from E_1 to E_2 (Fig. 2), the relative displacements of the five most displaced $\langle 111 \rangle$ atomic columns [61] are compared with the anisotropic elastic displacement field through the minimization of the cost function defined in Eq. (B.1) with respect to (x_1, y_1).

B.2. Disregistry function method

The disregistry corresponds to the displacement difference between the planes just above and below the dislocation glide plane. When fitting the disregistry, one has to take care of the way it is extracted from the atomistic calculations. Because of the atomic nature of matter, displacements can only be defined on discrete points. The upper and lower planes used to define the disregistry are located at a distance $\frac{h}{2}$ of the dislocation glide plane, where $h = a_0\frac{\sqrt{2}}{2}$ is the distance between {110} planes (Fig. B.13). One also needs to consider the offset $\varepsilon = a_0\frac{1}{\sqrt{6}}$ in the $\langle 211 \rangle$ glide direction corresponding to the distance
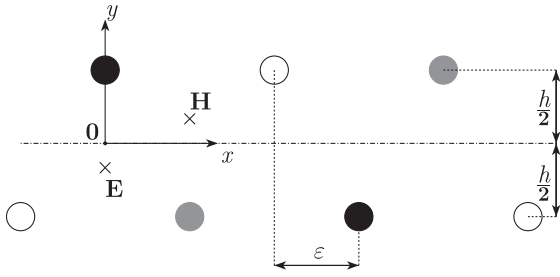
Fig. B.13. Sketch of the atomic planes used to calculate the disregistry. The easy-core position, denoted E, is located in $\left(0, -\frac{\sqrt{2}}{12}\right)$, and the hard-core position, denoted H, is located in $\left(\frac{1}{\sqrt{6}}, \frac{\sqrt{2}}{12}\right)$.

in the glide direction between two neighboring $\langle 111 \rangle$ atomic columns belonging to the upper and lower planes (Fig. B.13). We therefore define the disregistry as:

$$\Delta u_z^{\mathrm{at}}(x) = u_z^{\mathrm{at},+}\left(x + \frac{\varepsilon}{2}\right) - u_z^{\mathrm{at},-}\left(x - \frac{\varepsilon}{2}\right), \tag{B.2}$$

where $u_z^{\mathrm{at},+}(x)$ and $u_z^{\mathrm{at},-}(x)$ are displacements calculated respectively in the upper and lower planes.

To obtain a simple expression of the disregistry, we assume isotropic elasticity in the following. The displacement field of the screw dislocation along the Burgers vector direction is simply given by $u_z = b\frac{\theta}{2\pi}$. The angles of the two upper and lower atomic planes with respect to the cut plane are represented in Fig. B.14. For the dislocation D_1 located in (x_1, y_1), these angles are defined by:

$$\theta_1^+(x) = +\frac{\pi}{2} - \arctan\left(\frac{x - x_1}{\frac{h}{2} - y_1}\right) + \arctan\left(\frac{4y_1}{L}\right),$$
$$\theta_1^-(x) = -\frac{\pi}{2} + \arctan\left(\frac{x - x_1}{\frac{h}{2} + y_1}\right) + \arctan\left(\frac{4y_1}{L}\right), \tag{B.3}$$

where $y_1 = 0$ for the dislocation lying in its glide plane, i.e. at equal distance from the two neighboring {110} planes. The disregistry induced by this dislocation is given by:

$$\Delta u_{z,1}(x) = -\frac{b}{2\pi}\left[\theta_i^+\left(x + \frac{\varepsilon}{2}\right) - \theta_i^-\left(x - \frac{\varepsilon}{2}\right)\right]$$
$$= -\frac{b}{2} + \frac{b}{2\pi}\left[\arctan\left(\frac{2x - 2x_1 + \varepsilon}{h - 2y_1}\right)\right.$$
$$\left. + \arctan\left(\frac{2x - 2x_1 - \varepsilon}{h + 2y_1}\right)\right]. \tag{B.4}$$
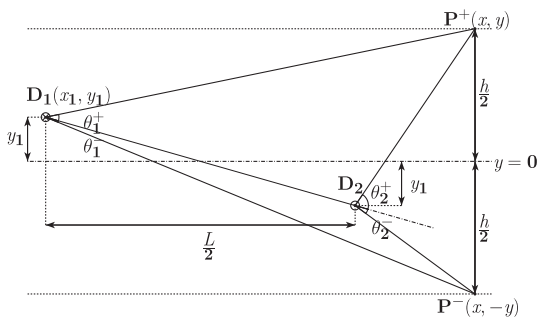

Fig. B.14. Definition of the angles for the two atomic planes immediately above and below the cut plane of the two dislocations constituting the dipole. P^+ and P^- belong to the upper and lower planes, respectively.
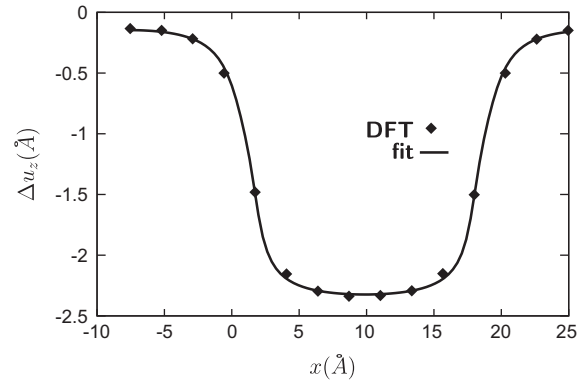

Fig. B.15. Disregistry in the z direction parallel to the Burgers vector, Δu_z, as a function of the dislocation-core position in the glide plane, x, halfway through the Peierls barrier. The diamonds denote the disregistry obtained from PWSCF GGA calculations using 135 atoms, and the line results from the adjustment through Eq. (B.6).

It should be noted that the angle gap in Eq. (B.3), $\theta_0 = \arctan\left(\frac{4y_1}{L}\right)$, comes from the angle of inclination between the cut plane and the {110} glide plane. Thus it vanishes within the differences $\theta_1^+ - \theta_1^-$ and this angle gap has no effect on the disregistry. Interestingly one obtains the same disregistry as predicted by the Peierls–Nabarro model, when the dislocation is exactly located in its glide plane ($y_1 = 0$), and when there is no offset in the $\langle 211 \rangle$ glide direction between atomic columns belonging to the upper and lower planes ($\varepsilon = 0$). Then the quantity $\frac{h}{2}$ corresponds to the dislocation spreading in the Peierls–Nabarro model.

Assuming that the distance in the glide plane between the two dislocations constituting the dipole is constant, the dislocation D_2 is located in $\left(x_1 + \frac{L}{2}, -y_1\right)$ (Fig. B.14). It induces a disregistry given by:

$$\Delta u_{z,2}(x) = +\frac{b}{2} - \frac{b}{2\pi}\left[\arctan\left(\frac{2x - 2x_1 - L + \varepsilon}{h + 2y_1}\right)\right.$$
$$\left. + \arctan\left(\frac{2x - 2x_1 - L - \varepsilon}{h - 2y_1}\right)\right]. \tag{B.5}$$

Finally, we take into account the fact that we have a periodic array of dislocation dipoles with period L along the x direction. The resulting disregistry function becomes:

$$\Delta u_z(x) = \sum_{n=-\infty}^{+\infty} [\Delta u_{z,1}(x - nL) + \Delta u_{z,2}(x - nL)]. \tag{B.6}$$

We end up with an expression of the disregistry function with two fitting parameters, x_1 and y_1, i.e. the dislocation core position in the (111) plane.

The resulting adjustment based on Eq. (B.6) halfway along the path is shown in Fig. B.15 using DFT atomic positions. The fitting expression accurately reproduces the disregistry computed from DFT calculations in the direction of the Burgers vector.

References

[1] Sesták B, Zárubová N, Sládek V. Can J Phys 1967;45:1031–40.
[2] Taoka T, Takeuchi S, Furubayashi E. J Phys Soc Jpn 1964;19:701–11.

[3] Furubayashi E. J Phys Soc Jpn 1969;27:130–46.
[4] Kubin LP, Louchet F. Acta Metall 1979;27:337–42.
[5] Christian JW. Metall Trans A 1983;14(7):1237–56.
[6] Kubin LP. Rev Deform Behav Mater 1976;1:244–88.
[7] Duesbery M. Dislocations in solids, vol. 8. Amsterdam: Elsevier; 1989.
[8] Caillard D. Acta Mater 2010;58:3493–503.
[9] Vitek V. Cryst Latt Def 1974;5:1–34.
[10] Duesbery MS, Basinski ZS. Acta Metall Mater 1993;41:643–7.
[11] Duesbery MS, Vitek V. Acta Mater 1998;46(5):1481–92.
[12] Chaussidon J, Fivel M, Rodney D. Acta Mater 2006;54:3407–16.
[13] Marian J, Cai W, Bulatov VV. Nat Mater 2004;3:158–63.
[14] Xu W, Moriarty JA. Phys Rev B 1996;54(10):6941–51.
[15] Rao SI, Woodward C. Philos Mag A 2001;81(5):1317–27.
[16] Yang LH, Söderlind P, Moriarty JA. Philos Mag A 2001;81(5):1355–85.
[17] Gilbert MR, Queyreau S, Marian J. Phys Rev B 2011;84:174103–11.
[18] Proville L, Rodney D, Marinica MC. Nat Mater 2012;11:845–9.
[19] Mrovec M, Nguyen-Manh D, Pettifor DG, Vitek V. Phys Rev B 2004;69(9):094115–16.
[20] Mrovec M, Nguyen-Manh D, Elsässer C, Gumbsch P. Phys Rev Lett 2011;106:246402–4.
[21] Ismail-Beigi S, Arias TA. Phys Rev Lett 2000;84(7):1499–502.
[22] Woodward C, Rao SI. Philos Mag A 2001;81(5):1305–16.
[23] Woodward C, Rao SI. Phys Rev Lett 2002;88(21):216402–4.
[24] Frederiksen SL, Jacobsen KW. Philos Mag 2003;83(3):365–75.
[25] Trinkle DR, Woodward C. Science 2005;310:1665–7.
[26] Domain C, Monnet G. Phys Rev Lett 2005;95(21). 215506–4.
[27] Romaner L, Ambrosch-Draxl C, Pippan R. Phys Rev Lett 2010;104:195503–4.
[28] Ventelon L, Willaime F. J Comput-Aid Mater Des 2007;14:85–94.
[29] Li H, Wurster S, Motz C, Romaner L, Ambrosch-Draxl C, Pippan R. Acta Mater 2012;60(17):748–58.
[30] Itakura M, Kaburaki H, Yamaguchi M. Acta Mater 2012;60:3698–710.
[31] Clouet E, Ventelon L, Willaime F. Phys Rev Lett 2009;102:055502–4.
[32] Takeuchi S, Kuramoto E. J Phys Soc Jpn 1975;38(2):480–7.
[33] Takeuchi S. Philos Mag A 1979;39(5):661–71.
[34] Zhao Y, Lu G. Modell Simul Mater Sci Eng 2011;19:065004–0650013.
[35] Cereceda D, Perlado JM, Queyreau S, Stukowski A, Marian J, Ventelon L, et al.; 2012. ArXiv:1204.5501v4.
[36] Samolyuk GD, Osetsky YN, Stoller RE. J Phys: Condens Matter 2013;25(2).
[37] Gilbert MR, Dudarev SL. Philos Mag 2010;90:1035–61.
[38] Gordon PA, Neeraj T, Li Y, Li J. Modell Simul Mater Sci Eng 2010;18:085008–0850013.
[39] Edagawa K, Suzuki T, Takeuchi S. Mater Sci Eng A 1997;234–236:1103–5.
[40] Edagawa K, Suzuki T, Takeuchi S. Phys Rev B 1997;55(10):6180–7.
[41] Segall DE, Strachan A, Goddard III WA, Ismail-Beigi S, Arias TA. Phys Rev B 2003;68(1):014104–0141011.
[42] Mendelev MI, Han S, Srolovitz DJ, Ackland GJ, Sun DY, Asta M. Philos Mag 2003;83(35):3977–94.
[43] Gordon PA, Neeraj T, Mendelev MI. Philos Mag 2011;91(30):3931–45.
[44] Giannozzi P, Baroni S, Bonini N, Calandra M, Car R, Cavazzoni C, et al. J Phys: Condens Matter 2009;21:395502–3955019.
[45] Soler JM, Artacho E, Gale JD, García A, Junquera J, Ordejón P, et al. J Phys: Condens Matter 2002;14:2745–79.
[46] Ventelon L, Willaime F. Philos Mag 2010;90:1063–74.
[47] Ventelon L, Willaime F, Fu CC, Heran M, Ginoux I. J Nucl Mater 2012;425:16–21.
[48] Cai W, Bulatov VV, Chang J, Li J, Yip S. Philos Mag 2003; 83(5):539–67.
[49] Clouet E. Phys Rev B 2011;84:224111–7.
[50] Clouet E, Ventelon L, Willaime F. Phys Rev B 2011; 84:224107–2241012.
[51] Li J, Wang CZ, Chang JP, Cai W, Bulatov VV, Ho KM, et al. Phys Rev B 2004;70(10):104113–8.
[52] Wang G, Strachan A, Çağin T, Goddard III WA. Phys Rev B 2003;67:140101–4.
[53] Cai W, Bulatov VV, Chang J, Li J, Yip S. Phys Rev Lett 2001; 86(25):5727–30.
[54] Henkelman G, Jóhannesson G, Jónsson H. Progress on theoretical chemistry and physics. Dordrecht: Kluwer Academic Publishers.; 2000.
[55] Henkelman G, Jónsson H. J Chem Phys 2000;113:9978–85.
[56] Rodney D. Phys Rev B 2007;76:144108–9.
[57] Rodney D, Proville L. Phys Rev B 2009;79:094108–9.
[58] Chiesa S, Derlet PM, Dudarev SL, Van Swygenhoven H. J Phys: Condens Matter 2011;23:206001–2060014.
[59] Wales DJ. Energy landscapes. Cambridge: Cambridge University Press; 2003.
[60] Aono Y, Kuramoto E, Kitajima K. Rep Res Inst Appl Mech 1981;XXIX:127–93.
[61] Gröger R, Vitek V. Modell Simul Mater Sci Eng 2012:20. 035019–13.
[62] Pizzagalli L, Beauchamp P, Jónsson H. Philos Mag 2008;88(1):91–100.
[63] Brunner D, Diehl J. Phys Stat Sol(a) 1997;160:355–72.
[64] Brunner D, Glebovsky V. Mater Lett 2000;42:290–6.
[65] Nguyen-Manh D, Horsfield AP, Dudarev SL. Phys Rev B 2006;73(2):020101–4.
[66] Odbadrakh K, Rusanu A, Stocks GM, Samolyuk GD, Eisenbach M, Wang Y, et al. J Appl Phys 2011;109. 07E159–4.
[67] Gröger R, Vitek V. Acta Mater 2008;56:5426–39.